Effective permeability of porous media containing branching channel networks

Michael J. Ronayne and Steven M. Gorelick
Department of Geological & Environmental Sciences, Stanford University, Stanford, California 94305-2115, USA
(Received 20 July 2005; revised manuscript received 5 December 2005; published 10 February 2006)

We study the effective permeability of two-dimensional binary systems characterized by a network of branching channels embedded in a uniform matrix material. Channels are assigned a higher permeability than the surrounding matrix and, therefore, serve as preferential pathways for fluid migration. The channel networks are constructed using a nonlooping invasion percolation model. We perform extensive numerical flow simulations to determine the effective permeability tensor of channel-matrix systems with broadly varying network properties. These computed effective permeabilities are then used to systematically investigate the factors that control the permeability upscaling process. The upscaling framework adopted for this study is based on spatial power averaging. We determine the scaling behavior of the averaging exponent ω by analyzing its dependence on three characteristic properties of the channel-matrix system: (i) the channel-matrix permeability contrast; (ii) the fractal dimension of the channel network, d_f; and (iii) the average tortuosity of spanning paths on the network backbone, τ. The behavior of ω and the corresponding component of effective permeability in each principal direction (parallel and perpendicular to the network-spanning direction) are compared. The permeability anisotropy ratio is shown to be a clear function of key system properties.

DOI: 10.1103/PhysRevE.73.026305 PACS number(s): 47.56.+r, 64.60.Ak

I. INTRODUCTION

Disordered geologic media often contain connected paths of high-permeability material that behave as preferred pathways for fluid flow and chemical migration. An active research area in subsurface science is aimed at developing a quantitative understanding of how these structural features influence macroscale flow and transport phenomena [1–5].

Percolation theory provides a useful framework for analyzing fluid-flow behavior in highly connected disordered media. Many studies in the percolation literature have explored the dependence of macroscopic dynamical quantities, such as effective permeability (or conductivity) [6,7] and tracer travel times [8,9] on various geometrical properties of percolation clusters. These investigations most often utilize the incipient spanning cluster (critical percolation cluster) as a representative structural model of the disordered porous medium. Critical path analysis (CPA), first proposed by Ambegaokar *et al.* [10], provides a basis for using a percolation cluster at criticality to study macroscopic flow behavior. The main argument supplied by CPA is that, in heterogeneous systems characterized by a broad distribution of permeabilities, the transport of fluids will be dominated by high-permeability regions. If the distribution of permeability values is very broad, areas having a permeability less than the critical value will not participate significantly in the transport. Therefore, the system may be minimally represented by a spanning percolation cluster that connects all locations having a permeability at least as high as the critical value. The dynamical model then involves flow across open bonds (or occupied lattice sites) on the cluster, with no flow occurring in the intercluster area, which is characterized by negligible permeabilities.

Traditional random percolation models, often used to represent strongly disordered media, assume that the nature of the spatial disorder is uncorrelated. In a site percolation problem, for example, this means the occupation probability for a given lattice site is not related to the occupancy status of its neighbor sites. The assumption of an uncorrelated or completely random medium tends to be justified for investigations of pore-scale dynamical processes. At the scale of individual pores, the degree of disorder (i.e., variability in pore conductances) is generally quite high [11], with negligible spatial correlation between neighboring regions of the medium. However, at larger length scales (e.g., field-scale subsurface systems on the order of tens to hundreds of meters), application of the random percolation model may no longer be warranted [12]. This is due to the fact that, in many subsurface geologic environments, the distribution of hydraulic properties (such as permeability) exhibits a significant amount of structure. For example, in geologic systems where material deposition was governed by fluvial processes, buried channel deposits commonly occur. Composed of coarse-grained porous material, these channels often form continuous high-permeability pathways that span large areas of the subsurface [13,14]. This and many other examples illustrate how processes active in the formation of geologic deposits can impart key structural patterns on the resulting hydraulic property distributions.

Recognizing the above geologic argument, some investigators have used spatially correlated percolation as a more realistic model for large-scale subsurface systems [15–18]. By introducing long-range spatial correlations in the lattice site occupation probabilities, critical percolation networks generated using this approach can better represent the geometry of high-permeability geobodies. As a result, spatially correlated networks may yield significantly improved estimates of macroscopic properties for many field settings. Regardless of the particular assumptions invoked concerning spatial correlation, the representation of porous media structure using a critical percolation network generally requires a sufficiently broad permeability distribution, in keeping with CPA.

In this paper, we consider an alternative percolation-based structural model of the porous medium that does not rely on the CPA argument. Our model is two dimensional (2D), although not limited to 2D, and consists of branching dendritic channels embedded in a low-permeability matrix material. The channel networks are generated using an invasion percolation algorithm. We focus on systems above the percolation threshold that are characterized by multiple spanning channels. For the purposes of this study, we assume a binary permeability distribution; that is, we assign one uniform permeability value along the channels and a different, lower value in the matrix area. Real geologic media are characterized by continuous rather than discrete (e.g., binary) hydraulic property distributions. However, ample evidence suggests that the permeability distribution in many sedimentary environments is bimodal [19–21] and that matrix regions, although less permeable, can significantly influence the flow behavior. For these bimodal sedimentary regimes, simplified models based on a binary permeability field can capture important characteristics of the fluid dynamics.

The channel-matrix conceptualization described in this paper is a useful heuristic model for studying dynamical processes in many natural systems that contain branching conduit geometries. Here, we consider porous subsurface environments spanned by high-permeability channel networks and focus our analysis on the effective permeability. By performing detailed flow simulations, we investigate the dependence of the effective permeability on key properties of the channel-matrix system, including geometrical properties of the channel network that are quantified using percolation concepts.

The remainder of this paper is organized into four additional sections. In Sec. II, we describe our methods for generating the channel networks and for characterizing important network properties that influence the flow behavior. In Sec. III, we outline the numerical flow simulation technique used to obtain an effective permeability for each channel-matrix system, and we present an upscaling framework to facilitate interpretation of the computed effective permeabilities. Section IV, the results section, contains our analysis of the sensitivity of effective permeability, and the fluid-flow behavior in general, to variations in key system properties. Finally, we discuss our conclusions in Sec. V.

II. CHANNEL NETWORK MODEL

A. Network generation

Our model for generating synthetic channel deposits is based on the work of Stark [22], who applied an invasion percolation model with a nonlooping constraint to simulate drainage networks. Stark and subsequent investigators [23] demonstrated that this model reproduces the observed fractal scaling properties of natural channel networks. We consider 2D site percolation on a square lattice. Implementation of the percolation model is as follows. First, a substrate strength value is assigned to each lattice site. Conceptually, the strength value is intended to represent the combined influence of various physical properties (e.g., topography, soil, and vegetation characteristics) on the likelihood of channel development at a particular location. We assign strength values randomly from a normal distribution. Network growth is initiated using one or more seed sites. Starting at the seed(s), neighboring sites with the lowest strength values are invaded (occupied). This process continues, with each new occupied site being part of a connected path that includes the seed site, until no additional growth is possible [Fig. 1(a)]. The nonlooping condition is implemented by never invading a new site that has occupied neighbors other than the source site from which growth is proceeding. A key component of our model is the specification of preferential growth factors that bias network development in particular directions. This aspect of the model permits the generation of channels with varying degrees of tortuosity, which is an important geometrical property that influences subsurface flow dynamics.

Figure 1 illustrates how the original percolation network is pruned to obtain the dendritic patterns that resemble natural channel networks. We use Strahler's method [24] to identify the order of each stream segment on the network. Labeling stream orders provides a convenient basis for controlling the proportion of channels in the channel-matrix system. We define a threshold stream order in the development of each channel network, such that all stream branches having an order lower than the threshold are pruned. When a higher threshold is specified, more extensive pruning occurs, resulting in a lower density of channels in the final system.

B. Characterization of key network properties

For each channel-matrix system evaluated in this study, we quantify two key geometrical properties of the (pruned) channel network that influence simulated flow behavior: (i) the network fractal dimension and (ii) the average channel tortuosity. We use the box-counting dimension to estimate the fractal dimension of the channel network, d_f. Figures 1(c) and 1(d) depict two networks with significantly different d_f values. Also reported with Fig. 1 is the range of box sizes used to compute d_f for the networks shown. The upper bound on this range (i.e., maximum box size implemented in the counting) represents a threshold with geometrical significance. For grids composed of square elements above this threshold size, all of the elements would be intersected by some part of the channel network. Subregions within a particular network domain tend to exhibit fractal scaling as their size increases beyond this identified threshold.

To calculate a meaningful tortuosity measure that captures the effect of channel tortuosity on the flow behavior, we focus on spanning paths that comprise the network backbone. The average spanning-path tortuosity computed for each network is defined by

$$\tau \equiv \frac{1}{B}\sum_{i=1}^{B} (l/r)_i \tag{1}$$

where B is the total number of spanning paths on the backbone, r is the Euclidean distance between starting and ending points on a given spanning path, and l is the path's actual distance. For loopless structures like the channel networks discussed here, the chemical or shortest path between two

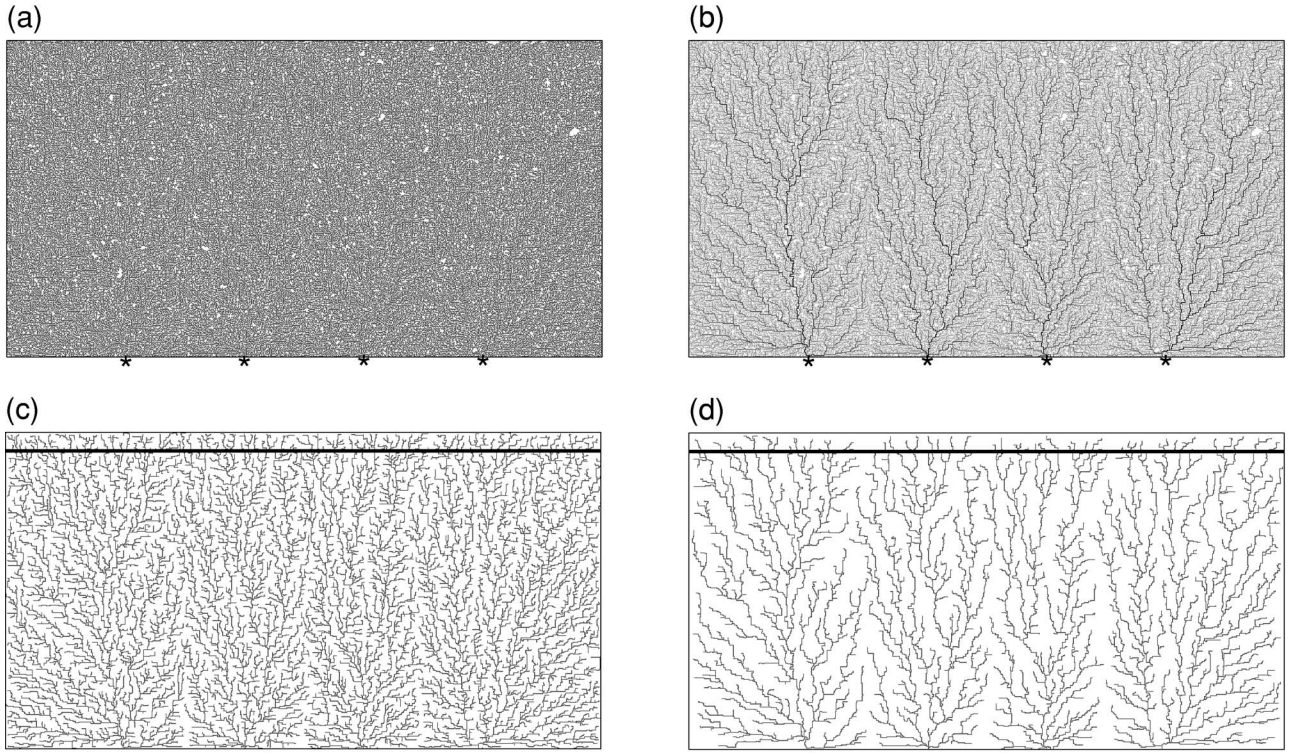

FIG. 1. (a) Typical percolation network prior to pruning. Lattice size is 425×800. Network development was initiated using four seed sites (marked by asterisks) along the bottom row. Unoccupied sites are shown in white. (b) Strahler stream orders for the same network. Darkest lines represent the highest-order streams. (c) Pruned network with lowest two stream orders removed. Fractal dimension (d_f) of this network is 1.41, estimated using box sizes (side lengths) ranging from 2 to 12. (d) Pruned network with three orders removed. Fractal dimension (d_f) is 1.26, with box sizes ranging from 2 to 20. The thick horizontal line shown in (c) and (d) is the upper boundary of the computational domain used for flow simulation. The size of the smaller rectangular area defined by this upper boundary is 400×800. The top 25 rows are cropped to ensure adequate spanning connectivity in the final domain.

boundary points represents the only path between those points.

In Fig. 2, percolation backbones are delineated for two channel networks characterized by different τ values. The τ values for all networks considered in this study range from 1.27 to 1.81. Strictly speaking, the transport backbone that we use to compute τ is only defined as such when the matrix permeability is zero. The structural model of interest in this study is a binary medium in which matrix throughflow is permitted. Nevertheless, we find the average spanning-path tortuosity to be an important geometrical property of the channel network. Intensive numerical simulations, the results of which will be discussed in Sec. IV, provide compelling evidence that τ is a key metric and that variations in τ have a predictable influence on the effective permeability over a broad range of channel-matrix permeability contrasts.

III. DETERMINATION OF EFFECTIVE PERMEABILITY

A. Flow simulation approach

We conducted detailed numerical simulations to determine the actual effective permeability for each channel-matrix system. Each 2D simulated system involves the steady-state, laminar flow of an incompressible fluid through a porous medium, which is described by [25]

$$\nabla \cdot q = \nabla \cdot \left(\frac{K}{\mu} \nabla \Psi \right) = 0, \tag{2}$$

where q is the specific discharge, Ψ is a fluid potential, μ is the dynamic viscosity of the fluid, and K is the permeability of the medium. The potential gradient can be expressed as $\nabla\Psi = \nabla(p + \rho g z)$, where p is the fluid pressure, ρ is the fluid density, g is the acceleration due to gravity, and z is elevation. We assume an incompressible fluid with constant density and viscosity. A complete description of the global effective permeability in our 2D channel-matrix systems requires a tensor

$$K_e = \begin{bmatrix} K_{e,xx} & 0 \\ 0 & K_{e,yy} \end{bmatrix}, \tag{3}$$

where $K_{e,xx}$ ($K_{e,yy}$) is the component of effective permeability in the x (y) direction. Off-diagonal elements in the above tensor are zero because the grid axes used to establish our simulation domain (labeled in Fig. 2) are oriented along the principal directions of anisotropy.

Specification of boundary conditions is necessary to obtain a solution to the steady-state flow equation. Prior to establishing these conditions and running the flow simulation, we first augment each channel-matrix system with homogeneous buffer zones at the top and bottom (when deter-

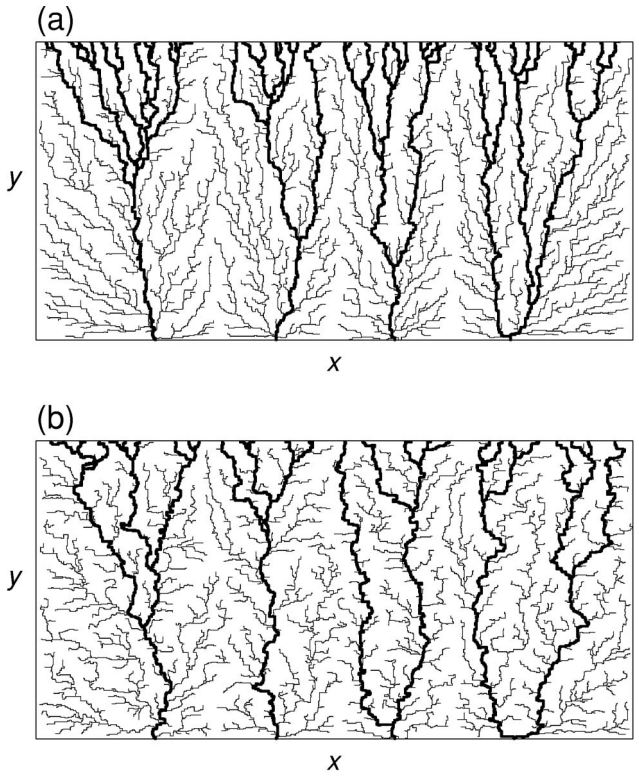

FIG. 2. Example networks showing subset of channels that comprise the percolation backbone. The backbone is defined by all channels that span the entire domain (spanning paths), connecting the upper and lower boundaries. Average spanning-path tortuosities (τ values) are 1.45 and 1.72, respectively, in (a) and (b).

mining $K_{e,yy}$) or along the left and right sides of the domain (when determining $K_{e,xx}$). The buffer zones are necessary to avoid simulating unrealistic flows near the inflow and outflow boundaries. The permeability value assigned to each buffer zone is the effective permeability of the channel-matrix system. Since this is the quantity that we would like to determine, its value is computed in an iterative fashion by performing multiple flow simulations. For flow in the y direction, we prescribe constant potentials at the top and bottom edges of the larger domain that includes buffer zones; this results in a gradient that drives flow through the system in the y direction. Zero-gradient conditions are implemented to represent impervious boundaries along the other two sides of the simulation domain. For flow in the x direction, constant potentials are specified along the edge of each buffer zone to the left and right, and the top and bottom boundaries are treated as impervious.

We numerically solve Eq. (2), subject to the aforementioned boundary conditions, using a finite-difference model. To obtain an accurate numerical solution that adequately resolves the highly nonuniform flow field observed in these systems, we develop a finely discretized model grid by subdividing each square lattice site into 16 smaller cells. The resulting computational domain, including the buffer zones, has over 10×10^6 nodes. We performed a systematic error analysis to arrive at this level of spatial discretization. Our approach was to increase the grid resolution until the calculated effective permeability (see below for calculation methodology) no longer changed significantly. This exercise was repeated using numerous permeability fields characterized by different network geometries. The enhanced spatial discretization used for the flow simulations has no impact on structural characteristics of the channel network; therefore, the values of d_f and τ remain unchanged.

From the fluid-potential distribution obtained by solving Eq. (2), we compute the global flow rate (Q_x or Q_y) through the system. The y component of effective permeability, $K_{e,yy}$, can be related to the rate Q_y using Darcy's law in the following form (e.g., Ref. [26]):

$$Q_y = -\frac{K_{e,yy}}{\mu}(L_x L_z)\frac{\Delta P}{L_y}, \quad K_{e,yy} = -\frac{Q_y L_y \mu}{(L_x L_z)\Delta P}, \tag{4}$$

where ΔP is the total potential drop across the system in the y direction (the macroscopic flow direction), L_x and L_y are the lattice sizes in the x and y directions, and L_z is the thickness of the section through which flow occurs (taken as unity). Similarly, when the applied potential gradient is in the x direction, Q_x is obtained and the effective permeability term is calculated as

$$K_{e,xx} = -\frac{Q_x L_x \mu}{(L_y L_z)\Delta P}. \tag{5}$$

The K values calculated using Eqs. (4) and (5) provide the effective permeability for an individual channel-matrix system. The key question addressed in this study is the following: How does that effective permeability depend on various system properties, such as geometrical properties of the channel network, d_f and τ, and the channel-matrix permeability contrast? We approach this question from an upscaling perspective.

B. Permeability upscaling

Numerous permeability upscaling methods have been developed and applied by investigators in statistical physics, groundwater hydrology, petroleum engineering, and related fields [27–30]. The method that we use in this study treats the upscaling problem as an averaging process. The objective is to average the local or point-scale permeability values in a manner that preserves the total flow through the volume of interest. That is, when the detailed local K distribution is replaced by the appropriate average value (or tensor component values), the same Q is produced if identical boundary conditions are applied. The permeability tensor that conserves mass is the effective permeability.

Our upscaling framework is based on spatial power averaging [31–33]. According to this method, each component of effective permeability can be calculated as a power average of the point-scale permeability values,

$$K_{e,ii} = \langle K^{\omega_i}\rangle^{1/\omega_i} = \left(\frac{1}{V}\int_V K(x,y)^{\omega_i} dV\right)^{1/\omega_i}, \tag{6}$$

where V is the averaging volume and $i=1$ or 2 refers to the directions x and y in our case. The averaging exponents ω_x and ω_y lie within the interval $[-1, 1]$. The limits on this interval correspond to the Wiener bounds

$$K_H \leq K_e \leq K_A, \tag{7}$$

meaning that each term in K_e is in the range bounded by the harmonic mean K_H and arithmetic mean K_A of the local permeabilities. For our binary channel-matrix systems, a simpler form of Eq. (6) is

$$K_{e,ii} = (f_m K_m^{\omega_i} + f_c K_c^{\omega_i})^{1/\omega_i}, \tag{8}$$

where K_m is the matrix permeability, K_c is the channel permeability, and f_m and f_c are the respective volume fractions occupied by each phase ($f_m + f_c = 1$).

For a given permeability field, the optimal value of ω will depend on the spatial distribution of local K values [29]. Instructive are two end-member hypothetical models, which have known ω values and involve fluid flow through 2D systems with perfectly layered media. When flow is parallel to the layering, the effective permeability is simply the arithmetic mean of the individual layer permeabilities, which corresponds to $\omega = 1$. When flow is normal to the layering, the effective permeability is given by the harmonic mean, corresponding to $\omega = -1$. The effective permeability is lower in the latter example because all of the fluid migrating through that system must traverse the least permeable layer(s). Consequently, the K_e value will be biased towards the lowest individual layer K. One other noteworthy 2D case is a permeability field where the $\log K$ distribution is described by a statistically homogeneous, multivariate Gaussian random function. The K_e in this case is the geometric mean K_G [34,35], which corresponds to ω near zero in Eq. (6) ($\lim_{\omega \to 0} = K_G$).

In the next section of this paper, we develop a predictive model that facilitates accurate determination of the averaging exponents (and therefore K_e) without resorting to exhaustive numerical simulation. More importantly, we demonstrate the dependence of the averaging exponent on salient properties that characterize each channel-matrix system. For this, we first need to calculate the observed values of ω_x and ω_y that yield the correct effective permeability for each system. We accomplish this by performing a flow simulation, calculating $K_{e,ii}$ using Eq. (4) or (5), and then solving the following optimization problem:

$$\min_{\omega_i \in [-1,1]} \{[(f_m K_m^{\omega_i} + f_c K_c^{\omega_i})^{1/\omega_i} - K_{e,ii}]^2\}. \tag{9}$$

By focusing on the ω_i value and relating it to the end-member permeabilities K_H and K_A, we consider how the averaging process is sensitive to key properties that distinguish our channel-matrix systems. Some previous investigators have noted that the averaging exponent is related to the degree of flow channeling (see Ref. [5] for a recent example). This is an important observation that informs our interpretation of the numerical results presented in Sec. IV. In essence, as the flow becomes more channelized, there is less sampling of the low-permeability matrix material, and therefore the appropriate average permeability increases towards the arithmetic mean (ω_i assumes its maximum value of 1 at $K_{e,ii} = K_A$).

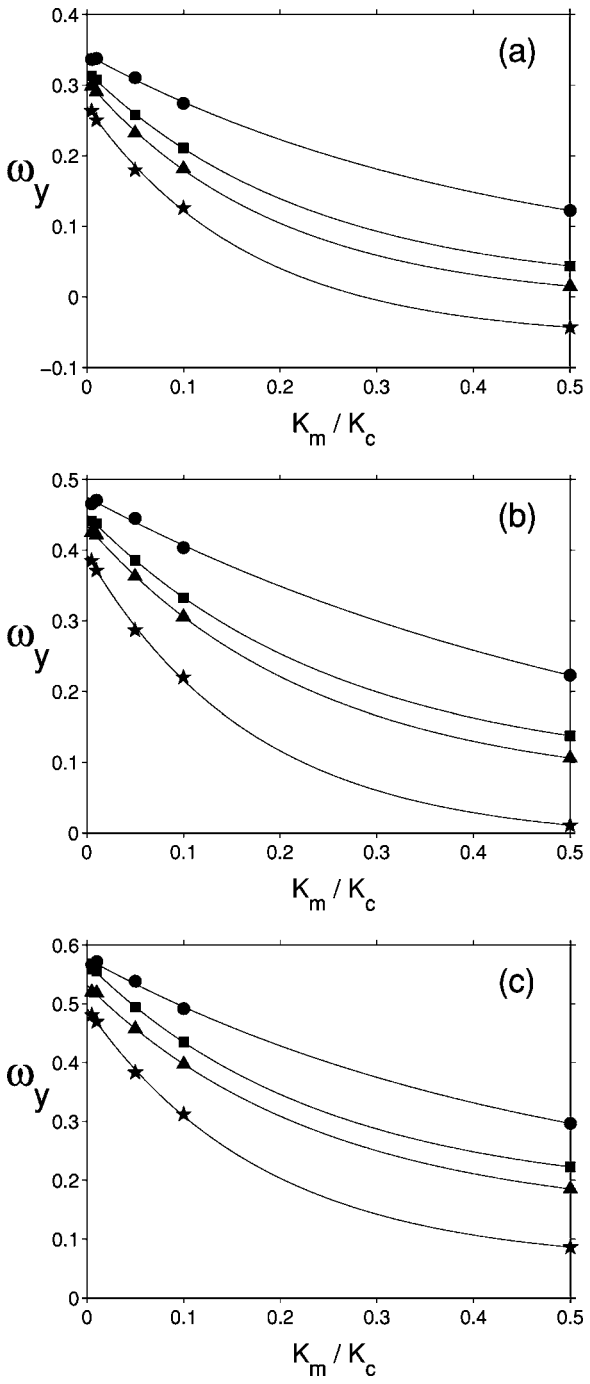

FIG. 3. Behavior of the averaging exponent ω_y as a function of permeability contrast. Each point corresponds to an observed value of ω_y for an individual channel-matrix system [obtained by solving Eq. (9)]. Points represented by the same symbol are from systems characterized by approximately equal d_f and τ values (i.e., the only significant difference within each grouping of points is the specified permeability contrast). Best-fit lines have an exponential form. (a) Results for systems with relatively high channel density ($d_f \approx 1.41$). (b) Results for medium-density systems ($d_f \approx 1.27$). (c) Results for low-density systems ($d_f \approx 1.16$).

IV. RESULTS

The results presented in this paper are based on flow simulations conducted for 150 distinct channel-matrix sys-

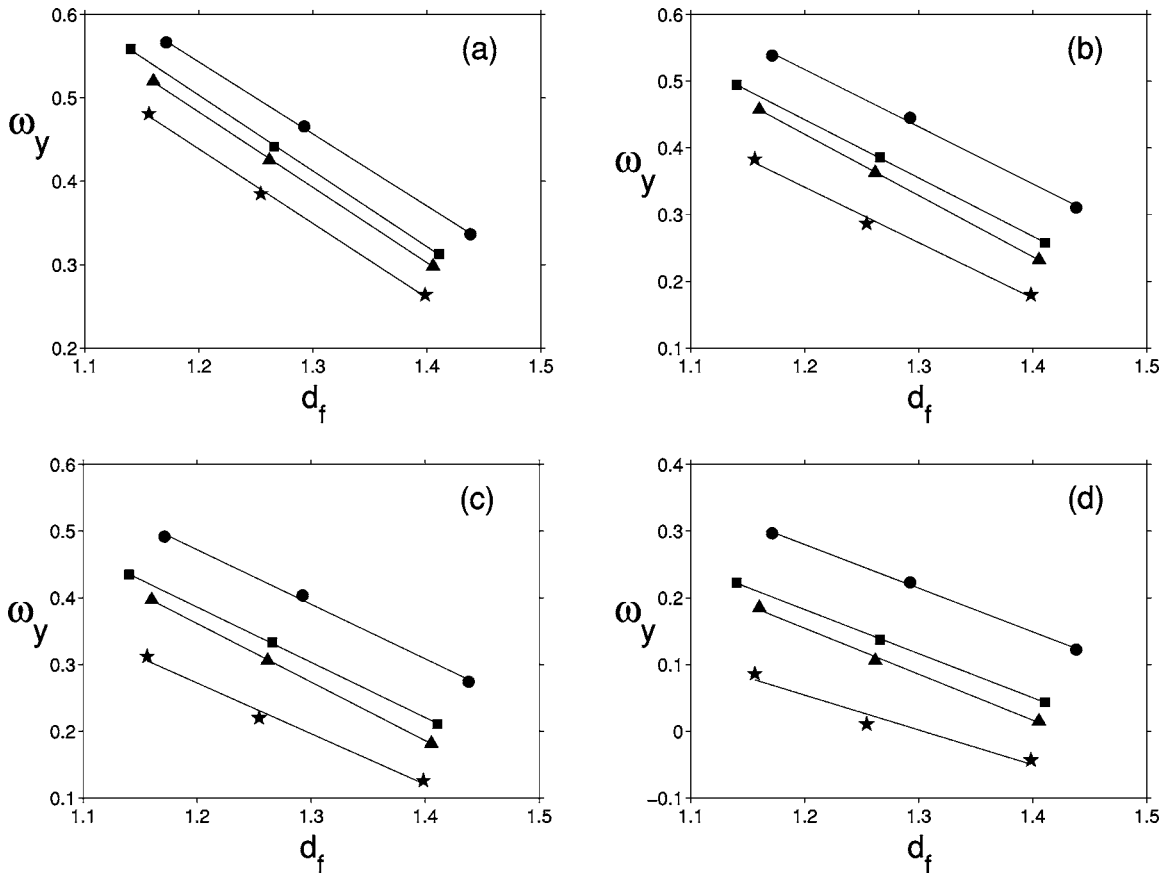

FIG. 4. Behavior of ω_y as a function of network fractal dimension. Points represented by the same symbol are from systems characterized by the same K_m/K_c ratio and approximately equal τ values (i.e., the only significant difference within each grouping of points is the d_f value). Straight lines represent the best linear fit. (a)–(d) show results for systems with differing permeability contrasts: (a) $K_m/K_c=0.005$, (b) $K_m/K_c=0.05$, (c) $K_m/K_c=0.1$, and (d) $K_m/K_c=0.5$.

tems. Each system is characterized by a unique set of values for the key variables, which are the channel-matrix permeability contrast and the geometric properties d_f and τ. In the first part of this section, we focus on the component of effective permeability in the y direction, which corresponds to the primary spanning direction of the anisotropic channel networks. An understanding of $K_{e,yy}$ is particularly important since preferential, rapid transport of fluids and chemicals is most likely to occur when the macroscopic gradient roughly coincides with the channel-spanning direction. We investigate the dependence of the averaging exponent ω_y on each of the three characteristic properties. After describing these dependencies in a quantitative manner, we then develop a predictive relationship for ω_y and use that relationship to calculate ω_y and $K_{e,yy}$ for all 150 channel-matrix systems. At the end of this section, we note the main controls on $K_{e,xx}$ and discuss the behavior of the anisotropy ratio $K_{e,xx}/K_{e,yy}$ with variations in the system properties.

The permeability contrast is defined using the ratio K_m/K_c. We fix the matrix permeability and vary the channel permeability to obtain the desired K contrast for each channel-matrix system. We consider a range of K_c values spanning two orders of magnitude. Within that range, the specific K_m/K_c ratios that we prescribe are 0.005, 0.01, 0.05, 0.1, and 0.5. Smaller values of the K_m/K_c ratio correspond to more extreme permeability contrasts. At $K_m/K_c=0.005$, for example, the channel permeability is 200 times greater than the matrix permeability.

Figure 3 shows the response of ω_y to variations in the permeability contrast. Results are presented for a representative subset of the 150 systems. The simulation results reveal an exponential relationship. We note that the averaging exponent scales as

$$\omega_y \sim \exp[(u)(K_m/K_c)], \tag{10}$$

where u yields a negative value and is reasonably approximated using a power law of the form $u(\tau)=\alpha\tau^{\beta}$ (α and β are constants, $\alpha<0, \beta>0$).

As the channel-matrix permeability contrast becomes more extreme, fluid flow is increasingly focused along the channels. This effect explains the trend of increasing ω_y with decreasing K_m/K_c shown in Fig. 3. The enhanced channeling means that less of the flow occurs within the low-permeability matrix. When matrix throughflow is reduced relative to the magnitude of flow in the channels, ω_y increases towards 1, its maximum theoretical value.

Next, we consider the dependence of ω_y on d_f, the fractal dimension of the channel network. The network development method used in this study, which involves the pruning of

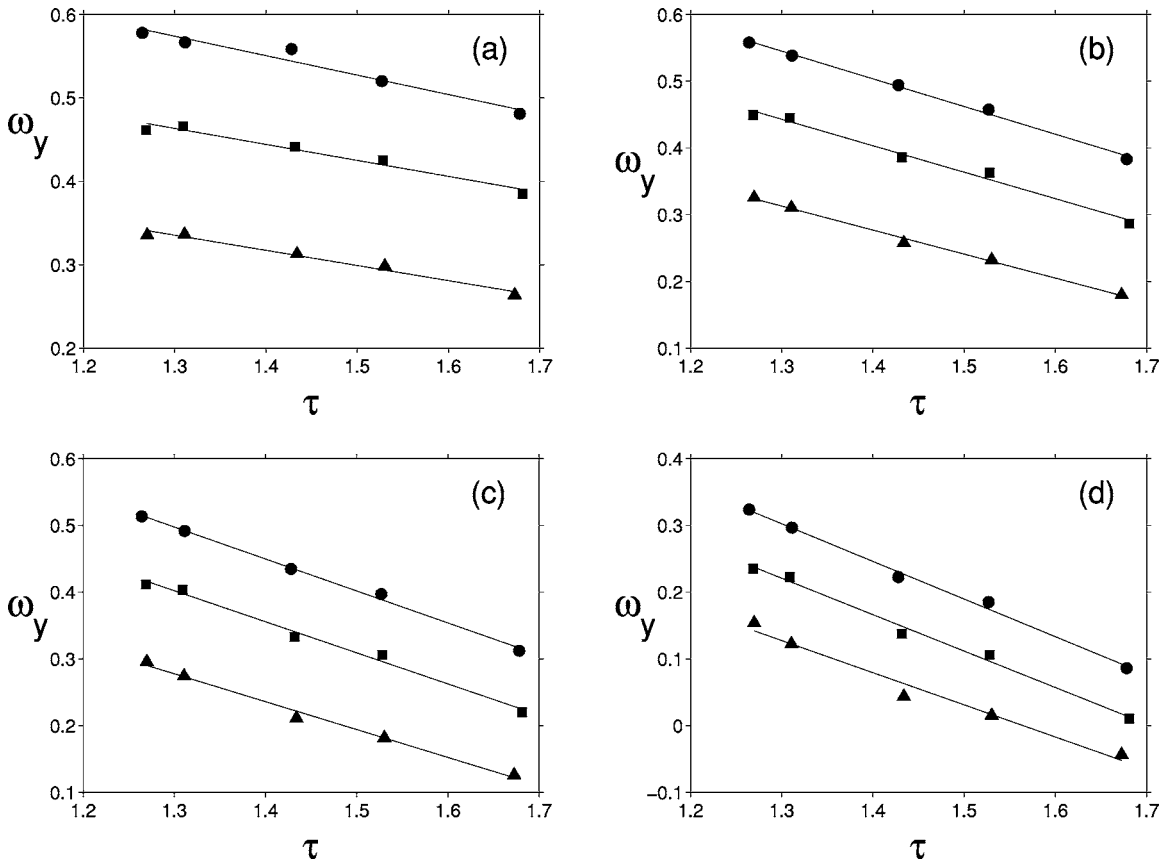

FIG. 5. Behavior of ω_y as a function of average spanning-path tortuosity. Points represented by the same symbol are from systems characterized by the same K_m/K_c ratio and approximately equal d_f values (i.e., the only significant difference within each grouping of points is the τ value). Straight lines represent the best linear fit. (a)–(d) show results for systems with differing permeability contrasts: (a) $K_m/K_c=0.005$, (b) $K_m/K_c=0.05$, (c) $K_m/K_c=0.1$, and (d) $K_m/K_c=0.5$.

selected channel segments according to a controllable threshold stream order, allows us to generate multiple networks with approximately the same spanning-path tortuosity τ, but different d_f values (Sec. II). As a result, we are able to systematically investigate the sensitivity of ω_y to variations in d_f only. The results presented in Fig. 4 indicate a strong linear dependence on the d_f value. As d_f increases, meaning that a larger fraction of the domain is occupied by channels, the value of the averaging exponent decreases. Retaining additional nonspanning channel segments results in a more diffuse (i.e., less channelized) flow field. This is a consequence of the imposed macroscopic flow direction, coupled with the particular fractal network geometry that we study. In a sense, all high-permeability channels throughout the domain have a tendency to "collect" the flow. Given the applied potential gradient, this effect can induce significant fluid flow through the matrix, particularly when a large number of low-order channels are present and serve as collectors.

Figure 5 shows the behavior of ω_y as a function of the average spanning-path tortuosity τ. Again, the functional relationship is linear. As the tortuosity increases, the value of the averaging exponent decreases. Interpretation of this result is aided by the following insight. At very high tortuosities, we would expect networks characterized by sinuous channels that migrate relatively large distances in the x direction compared to the distance covered in the spanning (y) direction. Given the applied boundary conditions which force flow in the y direction, this hypothetical high-tortuosity system resembles a layer-cake model where flow is normal to the layering ($K_e=K_H$ and $\omega=-1$ in that case). The averaging exponent is lower (toward the harmonic mean) at high tortuosities because a significant amount of the flow is being forced through the less permeable matrix material. At low tortuosities, channels are aligned more directly in the macroscopic gradient direction and the fluid tends to remain in those high-permeability features.

Another interesting result gleaned from inspection of Fig. 5 is that the averaging exponent is most sensitive to τ when the specified permeability contrast is close to 1 [e.g., Fig. 5(d)]. When the channel permeability is much larger than the matrix permeability ($K_m/K_c \ll 1$), ω_y is quite sensitive to d_f but only minimally influenced by the τ value [Fig. 5(a)].

One other important geometrical property that we have not yet addressed is the number of distinct spanning paths on the network. The frequency and spacing of high-permeability spanning paths clearly will have a significant impact on the flow dynamics. We find the number of seeds to be a reliable measure that captures this effect. Recall that we initiate the invasion percolation model using multiple seed locations, resulting in channel networks that consist of multiple treelike structures (Fig. 1). When more seeds are used to initiate network growth, there will be a higher frequency of spanning

paths in the resulting domain. The availability of such paths facilitates the channeling of fluid flow. Therefore, the averaging exponent should increase with the number of seeds. Indeed, this is what our flow simulations have revealed. We considered 75 two-seed systems and 75 four-seed systems. For similar values of K_m/K_c, d_f, and τ, the ω_y and $K_{e,yy}$ values are consistently higher in the channel-matrix systems that contain four-seed networks.

Based on the scaling behavior described by Eq. (10) and the additional linear dependencies highlighted in Figs. 4 and 5 ($\omega_y \sim 1/d_f$ and $\omega_y \sim 1/\tau$), we developed a model to predict the value of the averaging exponent using known values of K_m/K_c, d_f, and τ. Application of this simple nonlinear regression model resulted in strong agreement between predicted and observed values of ω_y over the entire range of the data; the overall r-squared value was 0.988. We then used the predicted values of ω_y to calculate a predicted $K_{e,yy}$ [Eq. (8)] for each channel-matrix system. Comparison of $\hat{K}_{e,yy}/K_G$ and $K_{e,yy}/K_G$ for each system, where $\hat{K}_{e,yy}$ denotes the predicted value, resulted in an r-squared value of 0.994. We normalize by the geometric mean to obtain a dimensionless measure of the effective permeability.

Thus far, we have discussed the factors that control effective permeability when the applied potential gradient is in the y direction, the network-spanning direction. We now consider the component of effective permeability in the x direction. The same general approach discussed previously for the y direction was used to determine values of $K_{e,xx}$ and ω_x for all 150 channel-matrix systems.

The averaging exponent ω_x exhibits the same exponential dependence on K_m/K_c that was observed for the y direction. That is, the scaling of ω_x with respect to permeability contrast is also described by the relationship given in Eq. (10). However, the β constant used in the estimation of u is negative when considering ω_x. The sensitivity to average spanning-path tortuosity is different in each direction. Whereas ω_y decreases with increasing τ, ω_x increases with increasing τ. This result is easily explained using the geometric argument presented earlier. At high tortuosities, the sinuous channels will provide convenient migration pathways for fluid flow in the x direction. Therefore, with increasing tortuosity, less of the flow is forced through the matrix, and the $K_{e,xx}$ value increases toward the arithmetic mean. At low tortuosities, a greater degree of matrix throughflow is required. The ω_x value demonstrates only a weak sensitivity to the fractal dimension d_f. In fact, we no longer observe a monotonic relationship between the averaging exponent and d_f for the x direction. At large permeability contrasts, ω_x decreases approximately linearly with increasing d_f, similar to the result observed for ω_y. However, for K_m/K_c near 1, there is actually a slight increase in the observed ω_x with increasing fractal dimension.

Figure 6 shows variations in the anisotropy ratio $K_{e,xx}/K_{e,yy}$ as a function of the permeability contrast and average spanning-path tortuosity. For most of the systems that we considered, and particularly for those with low d_f and τ values, $K_{e,xx}$ is less than $K_{e,yy}$. As shown in Fig. 6, the ratio $K_{e,xx}/K_{e,yy}$ increases with increasing τ. This is consistent with the observed dependencies for the averaging exponents

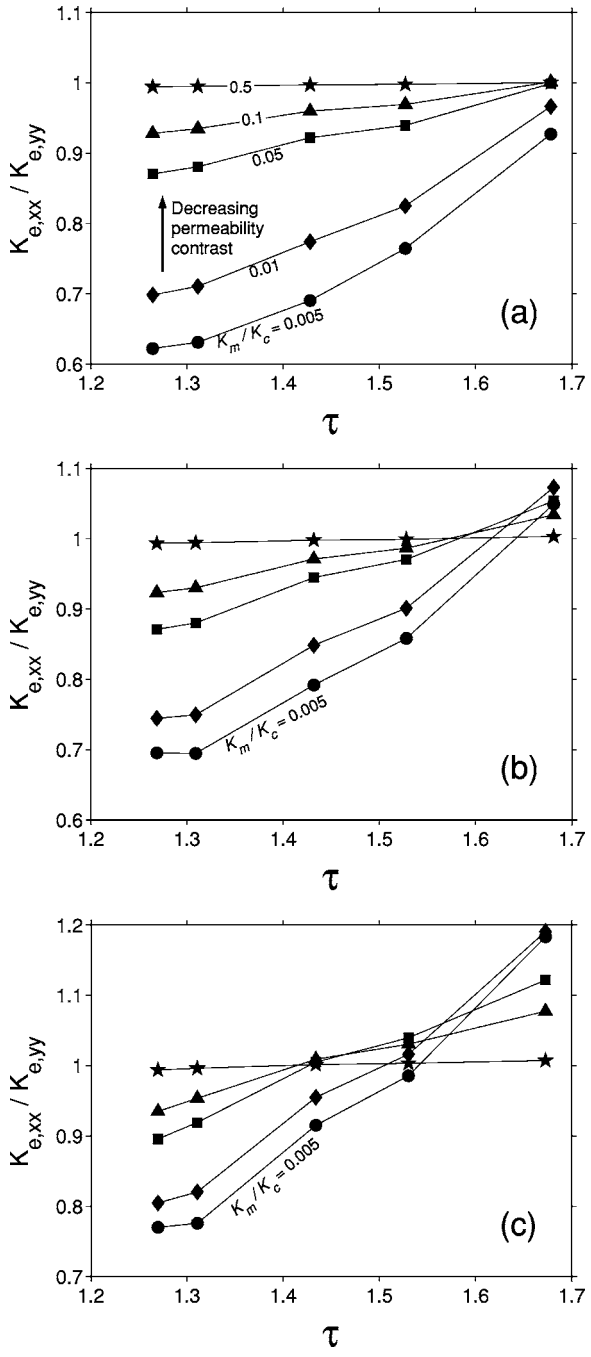

FIG. 6. Anisotropy ratio, $K_{e,xx}/K_{e,yy}$, plotted as a function of the average spanning-path tortuosity (recall that τ is measured in the y direction). Points represented by the same symbol are from systems with the same permeability contrast. (a) Results for systems with low channel density ($d_f \approx 1.16$). (b) Results for medium-density systems ($d_f \approx 1.27$). (c) Results for high-density systems ($d_f \approx 1.41$). The numbers labeling each line in (a) give the K_m/K_c ratio for that set of five points; these ratios also apply to the corresponding sets in (b) and (c).

(i.e., ω_x increases and ω_y decreases with increasing τ). For channel-matrix systems with a relatively low fraction of channels (low d_f), $K_{e,xx}$ is consistently less than $K_{e,yy}$ [Fig. 6(a)]. However, $K_{e,xx}$ is sometimes greater than $K_{e,yy}$ for systems with moderate to high channel fraction [Figs. 6(b) and

6(c)]. When the channel volume fraction is sufficiently large and the channels are characterized by high tortuosity (recall that τ is measured in the y direction), there may be less resistance to flow in the x direction as compared to the spanning (y) direction. In particular, the ratio $K_{e,xx}/K_{e,yy}$ is likely to exceed 1 in systems characterized by high d_f and τ values.

V. CONCLUDING REMARKS

Here, we investigated the effective permeability of binary systems consisting of a branching channel network embedded in a low-permeability matrix. To construct the channel networks, we used a nonlooping invasion percolation model modified to implement preferred directional growth factors, an approach that allowed us to generate numerous networks with varying geometrical properties. We focused on two key properties that have a significant and predictable influence on fluid flow behavior: the fractal dimension and the average spanning-path tortuosity. In addition to variations in these network properties, we also evaluated a relatively broad range of channel-matrix permeability contrasts. Numerical flow simulations were conducted to determine accurate values of the effective permeability and power averaging exponents [ω_i in Eqs. (6), (8), and (9)] for each channel-matrix system; these simulated data were then used to analyze the dependence of ω_i on the key system properties.

The effective permeability in our 2D channel-matrix systems is described by a diagonal tensor [Eq. (3)] for the coordinate axes that we selected. For all but 3 of the 150 systems evaluated in this study, the component of effective permeability in the network-spanning direction, $K_{e,yy}$, was between the geometric and arithmetic mean permeability values, a range corresponding to the interval [0, 1] for the averaging exponent ω_y. We determined the following specific dependencies for the averaging exponent: (i) ω_y increases exponentially as the channel permeability is increased relative to the matrix permeability [the scaling relation for this exponential dependence is given by Eq. (10)]; (ii) ω_y increases linearly as the fractal dimension of the channel network, d_f, decreases; and (iii) ω_y increases linearly as the average spanning-path tortuosity τ decreases. These dependencies are clear over the range of system property values that we considered. We also studied the component of effective permeability in the x direction, $K_{e,xx}$; this value exceeded the geometric mean permeability in all but 13 of the 150 systems. The corresponding averaging exponent ω_x increases in an exponential fashion with increasing channel-matrix permeability contrast, a relationship similar to the one observed for ω_y. Unlike in the y direction, ω_x increases as τ increases. Therefore, the anisotropy ratio $K_{e,xx}/K_{e,yy}$ increases with increasing channel tortuosity. The largest anisotropy ratios are observed for systems characterized by high d_f and τ values.

Our results suggest that the averaging exponent is a useful dimensionless parameter related to the degree of flow channeling. Consequently, we note that, in addition to providing a predictive framework for permeability upscaling in structurally heterogeneous fields, application of the spatial power averaging method can give insight into the nature of the flow dynamics.

ACKNOWLEDGMENTS

The first author gratefully acknowledges the support of the U.S. Department of Defense. Additional funding for this work was provided by the National Science Foundation under Grant Nos. EAR-0003511, EAR-0003914, EAR-0537668, and EAR-0538011. Any opinions, findings, and conclusions or recommendations expressed in this material are those of the authors and do not necessarily reflect the views of the National Science Foundation.

[1] R. Wallach, T. S. Steenhuis, and J.-Y. Parlange, in *The Handbook of Groundwater Engineering*, edited by J. W. Delleur (CRC Press, Boca Raton, 1999).
[2] A. W. Western, G. Blöschl, and R. B. Grayson, Water Resour. Res. **37**, 83 (2001).
[3] C. Zheng and S. M. Gorelick, Ground Water **41**, 142 (2003).
[4] B. Zinn and C. F. Harvey, Water Resour. Res. **39**, 4-1 (2003).
[5] C. Knudby and J. Carrera, Adv. Water Resour. **28**, 405 (2005).
[6] S. Havlin and D. Ben-Avraham, Adv. Phys. **36**, 695 (1987).
[7] D. Stauffer and A. Aharony, *Introduction to Percolation Theory* (Taylor & Francis, Philadelphia, 1994).
[8] Y. Lee, J. S. Andrade, Jr., S. V. Buldyrev, N. V. Dokholyan, S. Havlin, P. R. King, G. Paul, and H. E. Stanley, Phys. Rev. E **60**, 3425 (1999).
[9] J. S. Andrade, Jr., S. V. Buldyrev, N. Dokholyan, S. Havlin, P. R. King, Y. Lee, G. Paul, and H. E. Stanley, Phys. Rev. E **62**, 8270 (2000).
[10] V. Ambegaokar, B. I. Halperin, and J. S. Langer, Phys. Rev. B **4**, 2612 (1971).
[11] C. B. Shah and Y. C. Yortsos, Phys. Fluids **8**, 280 (1996).
[12] A. G. Hunt, Adv. Water Resour. **24**, 279 (2001).
[13] C. E. Koltermann and S. M. Gorelick, Water Resour. Res. **32**, 2617 (1996).
[14] G. E. Fogg, S. F. Carle, and C. Green, in *Theory, Modeling, and Field Investigation in Hydrogeology: A Special Volume in Honor of Shlomo P Neuman's 60th Birthday*, edited by D. Zhang and C. L. Winter (Geological Society of America, Boulder, CO, 2000).
[15] S. Prakash, S. Havlin, M. Schwartz, and H. E. Stanley, Phys. Rev. A **46**, R1724 (1992).
[16] C. Du, C. Satik, and Y. C. Yortsos, AIChE J. **42**, 2392 (1996).
[17] H. A. Makse, J. S. Andrade, Jr., and H. E. Stanley, Phys. Rev. E **61**, 583 (2000).
[18] A. D. Araújo, A. A. Moreira, H. A. Makse, H. E. Stanley, and J. S. Andrade, Jr., Phys. Rev. E **66**, 046304 (2002).
[19] A. J. Desbarats, Water Resour. Res. **26**, 153 (1990).
[20] S. Bachu, Tectonophysics **190**, 299 (1991).
[21] R. W. Ritzi *et al.*, Water Resour. Res. **36**, 3179 (2000).
[22] C. P. Stark, Nature (London) **352**, 423 (1991).
[23] M. Cieplak, A. Giacometti, A. Maritan, A. Rinaldo, I.

Rodriguez-Iturbe, and J. R. Banavar, J. Stat. Phys. **91**, 1 (1998).
[24] A. N. Strahler, Trans., Am. Geophys. Union **38**, 913 (1957).
[25] S. E. Ingebritsen and W. E. Sanford, *Groundwater in Geologic Processes* (Cambridge University Press, Cambridge, England, 1998).
[26] E. L. Hinrichsen, A. Aharony, J. Feder, A. Hansen, and T. Jøssang, Transp. Porous Media **12**, 55 (1993).
[27] P. R. King, Transp. Porous Media **4**, 37 (1989).
[28] X. H. Wen and J. J. Gómez-Hernández, J. Hydrol. **183**, 9 (1996).
[29] P. Renard and G. de Marsily, Adv. Water Resour. **20**, 253 (1997).
[30] C. L. Farmer, Int. J. Numer. Methods Fluids **40**, 63 (2002).
[31] A. G. Journel, C. Deutsch, and A. J. Desbarats, in Proceedings 15091–15149, 56th Annual California Regional Meeting, Society of Petroleum Engineers, Oakland, California 1986 (Soc. of Petroleum Engineers, Richardson, TX 1986), Vol. 2, pp. 329–334.
[32] C. Deutsch, SPE Form. Eval. **4**, 343 (1989).
[33] A. J. Desbarats, Math. Geol. **24**, 249 (1992).
[34] G. Matheron, *Eléments pour une Théorie des Milieux Poreux* (Masson, Paris, 1967).
[35] G. Dagan, Water Resour. Res. **15**, 47 (1979).